Lagrangian coherent structures at the onset of hyperchaos in the two-dimensional Navier-Stokes equations

Rodrigo Miranda, Erico Rempel, Abraham C.-L. Chian, Norbert Seehafer, Benjamin Toledo, Pablo Muñoz

Lagrangian coherent structures at the onset of hyperchaos in the two-dimensional Navier-Stokes equations

Rodrigo A. Miranda,[1,2,a)] Erico L. Rempel,[2,3] Abraham C.-L. Chian,[2,3,4] Norbert Seehafer,[5] Benjamin A. Toledo,[2,6] and Pablo R. Munoz[2]

[1]University of Brasılia (UnB), Faculty UnB-Gama, and Plasma Physics Laboratory, Institute of Physics, Brasılia, DF 70910-900, Brazil
[2]Institute of Aeronautical Technology (ITA) and World Institute for Space Environment Research (WISER), Sao Jose dos Campos, SP 12228-900, Brazil
[3]National Institute for Space Research (INPE) and World Institute for Space Environment Research (WISER), PO Box 515, Sao Jose dos Campos, SP 12227-010, Brazil
[4]Observatoire de Paris, LESIA, CNRS, 92195 Meudon, France
[5]Institut für Physik und Astronomie, Universität Potsdam, Karl-Liebknecht-Str. 24/25, 14476 Potsdam, Germany
[6]Department of Physics, Faculty of Sciences, University of Chile, P. O. Box 653, Santiago, Chile

We study a transition to hyperchaos in the two-dimensional incompressible Navier-Stokes equations with periodic boundary conditions and an external forcing term. Bifurcation diagrams are constructed by varying the Reynolds number, and a transition to hyperchaos (HC) is identified. Before the onset of HC, there is coexistence of two chaotic attractors and a hyperchaotic saddle. After the transition to HC, the two chaotic attractors merge with the hyperchaotic saddle, generating random switching between chaos and hyperchaos, which is responsible for intermittent bursts in ts of the flow are characterized by detecting Lagrangian coherent structures. After the transition to HC, the flow displays complex Lagrangian patterns and an increase in the level of Lagrangian chaoticity during the bursty periods that can be predicted statistically by the hyperchaotic saddle prior to HC transition.

The Lagrangian approach to the characterization of the transport and mixing properties of fluids in terms of coherent structures has attracted much attention in recent years. In this paper, we focus on the chaotic mixing properties of a two-dimensional (2D) incompressible flow in a crisis-like transition to hyperchaos (HCs). First, we construct bifurcation diagrams and detect chaotic saddles at the onset of hyperchaos, using a fixed frame of reference in Fourier space (i.e., an Eulerian approach). Next, we characterize the chaotic mixing properties of the fluid by detecting Lagrangian coherent structures (LCSs). We show that, prior to the transition, chaotic saddles can be used to predict the enhanced complexity of the spatiotemporal patterns observed in the hyperchaotic regime.

I. INTRODUCTION

Numerical studies of nonlinear systems modelled by partial differential equations show that they may exhibit a crisis like transition involving random switches between periods of transient temporal chaos (TC) and spatiotemporal chaos (STC). TC refers to the regime in which the patterns of the numerical solution are chaotic in time and regular in space, and is characterized by a low fractal dimension,[1,2] narrow band power spectrum,[3] and one positive Lyapunov exponent.[2] STC refers to the regime in which the patterns are chaotic in time and disordered in space, and is character ized by a high fractal dimension,[1,2] broad band power spec trum,[3] and the presence of hyperchaos (i.e., two or more positive Lyapunov exponents).[2] The coupling between two chaotic saddles was shown to be responsible for the TC STC intermittency.[1,4] Chaotic saddles are nonattracting chaotic sets responsible for transient chaos.[5–8] A thorough overview on the subject of transient chaos and its applications can be found in the recent monograph by Lai and Tél.[9]

In this paper, we study the dynamics of two dimensional incompressible flows modelled by the 2D Navier Stokes equations (2D NSE) with an external forcing term and peri odic boundary conditions. These equations can be solved numerically with the spectral method by transforming the equations to Fourier space, and truncating the Fourier series to a finite number of modes for the numerical implementa tion. This method has been used in a series of works to study the transition from a laminar state to a chaotic regime. Boldrighini and Franceschini[10] first showed that the numeri cal solutions of a 5 mode truncation of the 2D NSE can ex hibit chaotic behavior arising from a series of bifurcations observed with increasing values of the Reynolds number. Lee[11] presented a detailed work on the complex route from laminar to chaotic behavior by varying the Reynolds number and strength of the forcing term, and compared the effect of the external force acting on a single mode and on multiple modes in Fourier space. A systematic study of the transition to chaos in the 2D NSE was presented by Feudel and Seehafer.[12,13] They characterized a wealth of regimes with

[a)]Electronic mail: rmiracer@unb.br

increasing amplitude of the forcing term, including steady states with broken symmetries, travelling waves, modulated travelling waves, torus and chaos, and compared the influence of these regimes on the trajectory of a test particle in real space. The transition to chaos and the mixing properties of the 2D NSE were also examined by Braun *et al.*[14] They analyzed the evolution of a set of tracer particles in the presence of an external forcing consisting of an array of vortices, and demonstrated that the rate of stretching of the initial patch of tracers is stronger in the chaotic and quasiperiodic regimes and is weaker in the periodic and laminar regimes. Braun *et al.*[15] compared numerical simulations of the 2D NSE using stress free and no slip boundary conditions in the vertical direction, and periodic boundary conditions in the horizontal direction. They found that the bifurcation scenario is relatively robust to changes of the boundary conditions, and that the final route to chaos in the 2D NSE with stress free boundary conditions occurs by a period doubling cascade, whereas the destruction of a two frequency torus may be responsible for the onset of chaos in the no slip case. The transition to chaos of a two dimensional flow confined on a square domain with no slip walls was explored by Molenaar *et al.*[16] They found that the route to chaos corresponds to the Ruelle Takens Newhouse scenario[17,18] and the flow is dominated by a large circulation cell in real space.

The Lagrangian description of fluids has attracted much attention during the past decade because it can provide a consistent definition of coherent structures in turbulent flows,[19] and as a result, several concepts and new techniques have been developed to detect them. In this paper, we use chaotic saddles to explain the spatiotemporal patterns observed in numerical simulations of the 2D NSE at the onset of hyperchaos, and their role on the chaotic advection of tracer particles by computing the maximum finite time Lyapunov exponent (FTLE) which is a popular tool for detecting LCSs,[21,22] and a mathematical theory recently developed[23,24] to obtain hyperbolic LCSs as smooth, parametrized curves in 2D flows.

This paper is organized as follows. The derivation of the spectral form of the 2D NSE and the details of the numerical implementation are presented in Sec. II. The Lagrangian techniques used to characterize the transport of particles are briefly reviewed in Sec. III. Our numerical analysis begins in Sec. IV, where we identify a crisis like transition to hyperchaos and detect chaotic saddles in a fixed frame of reference in Fourier space (i.e., the Eulerian approach). In Sec. V, we combine the Eulerian bifurcation scenario with the phenomenology of chaotic advection using the Lagrangian approach. Finally, we present our conclusion and discuss the application of our results for the understanding of chaotic mixing observed in the atmosphere and the oceans in Sec. VI.

II. THE 2D NAVIER-STOKES EQUATIONS

The dynamics of two dimensional incompressible fluids are governed by the Navier Stokes equations, which in non dimensional form are[12]

$$\partial_t \mathbf{u} + (\mathbf{u}\cdot\nabla)\mathbf{u} = -\nabla p + \frac{1}{\mathrm{Re}}\nabla^2\mathbf{u} + \mathbf{f}, \tag{1}$$

$$\nabla\cdot\mathbf{u} = 0, \tag{2}$$

where $\mathbf{u} = \mathbf{u}(\mathbf{x},t) = (u_x(\mathbf{x},t), u_y(\mathbf{x},t))$ denotes the fluid velocity, $\mathbf{x} = (x, y)$ is the position vector in the fixed frame of reference, and $p = p(\mathbf{x}, t)$ is the pressure, Re represents the Reynolds number, and $\mathbf{f} = (f_x(\mathbf{x},t), f_y(\mathbf{x},t))$ represents an external force. In the Fourier representation, we can write $\mathbf{u}$, p, and $\mathbf{f}$ as

$$\mathbf{u}(\mathbf{x},t) = \sum_{\substack{\mathbf{k}\in\mathbb{Z}^2,\\ \mathbf{k}\neq 0}} \hat{\mathbf{u}}_{\mathbf{k}}(t) e^{i\mathbf{k}\cdot\mathbf{x}}, \tag{3}$$

$$p(\mathbf{x},t) = \sum_{\substack{\mathbf{k}\in\mathbb{Z}^2,\\ \mathbf{k}\neq 0}} \hat{p}_{\mathbf{k}}(t) e^{i\mathbf{k}\cdot\mathbf{x}}, \tag{4}$$

$$\mathbf{f}(\mathbf{x},t) = \sum_{\substack{\mathbf{k}\in\mathbb{Z}^2,\\ \mathbf{k}\neq 0}} \hat{\mathbf{f}}_{\mathbf{k}}(t) e^{i\mathbf{k}\cdot\mathbf{x}}, \tag{5}$$

where the hat indicates the complex Fourier coefficient of the corresponding quantity, $\mathbf{k} = (k_x, k_y)$ is the wavevector, $k_x = 2\pi n_x/L_x$, $k_y = 2\pi n_y/L_y$, $n_x, n_y \in \mathbb{Z}$, and $i = \sqrt{-1}$. In this paper, we assume $L_x = L_y = 2\pi$ and periodic boundary conditions in the x and y directions, hence $\mathbf{k}\in\mathbb{Z}^2$. The restriction $\mathbf{k}\neq 0$ arises from the fact that $\hat{\mathbf{u}}_0$ is decoupled from the evolution equations, which is demonstrated in Appendix A. Inserting Eqs. (3) (5) into Eq. (1), we obtain

$$\frac{d\hat{\mathbf{u}}_{\mathbf{k}}}{dt} = -i\mathbf{k}\hat{p}_{\mathbf{k}} - \frac{1}{\mathrm{Re}}k^2\hat{\mathbf{u}}_{\mathbf{k}} + \hat{\mathbf{f}}_{\mathbf{k}} - i\sum_{\substack{\mathbf{p}\in\mathbb{Z}^2,\\ \mathbf{p}\neq 0,\mathbf{k}}} (\hat{\mathbf{u}}_{\mathbf{p}}\cdot\mathbf{k})\hat{\mathbf{u}}_{\mathbf{k}-\mathbf{p}}. \tag{6}$$

Inserting Eq. (3) into Eq. (2), the incompressibility requirement takes the form:

$$\hat{\mathbf{u}}_{\mathbf{k}}(t)\cdot\mathbf{k} = 0. \tag{7}$$

Note from Eq. (7) that the incompressibility in Fourier space restricts the dynamics of the Fourier modes $\hat{\mathbf{u}}_{\mathbf{k}}$ to the direction perpendicular to the wavevector $\mathbf{k}$. To impose this restriction, we define a real unit vector $\mathbf{e}_{\mathbf{k}}$ perpendicular to $\mathbf{k}$[11–13]

$$\mathbf{e}_{\mathbf{k}}\cdot\mathbf{k} = 0, \qquad e_{\mathbf{k}}^2 = \mathbf{e}_{\mathbf{k}}\cdot\mathbf{e}_{\mathbf{k}} = 1, \qquad \mathbf{e}_{-\mathbf{k}} = \mathbf{e}_{\mathbf{k}}, \tag{8}$$

and project the velocity in Fourier space along the vector $\mathbf{e}_{\mathbf{k}}$

$$\hat{\mathbf{u}}_{\mathbf{k}} = \hat{u}_{\mathbf{k}}\mathbf{e}_{\mathbf{k}}, \tag{9}$$

where $\hat{u}_{\mathbf{k}} = u_{\mathbf{k}}^R + iu_{\mathbf{k}}^I$ is a complex scalar quantity. As a result, the complex two dimensional vector $\hat{\mathbf{u}}_{\mathbf{k}}$ is reduced to a complex one dimensional (i.e., scalar) quantity $\hat{u}_{\mathbf{k}}$ because $\hat{\mathbf{u}}_{\mathbf{k}}$ vanishes in the direction parallel to $\mathbf{k}$.[12,13] Substituting Eq. (9) into Eq. (6) and projecting the resulting equation into $\mathbf{e}_{\mathbf{k}}$, we obtain

$$\frac{d\hat{u}_{\mathbf{k}}}{dt} = -\frac{1}{\mathrm{Re}}k^2\hat{u}_{\mathbf{k}} + \hat{f}_{\mathbf{k}} - i\sum_{\substack{\mathbf{p}\in\mathbb{Z}^2,\\ \mathbf{p}\neq 0,\mathbf{k}}} (\mathbf{e}_{\mathbf{p}}\cdot\mathbf{k})(\mathbf{e}_{\mathbf{k}-\mathbf{p}}\cdot\mathbf{e}_{\mathbf{k}})\hat{u}_{\mathbf{p}}\hat{u}_{\mathbf{k}-\mathbf{p}}, \tag{10}$$

where $\hat{f}_{\mathbf{k}} = \hat{\mathbf{f}}_{\mathbf{k}} \cdot \mathbf{e}_{\mathbf{k}}$. Note that the pressure term vanishes. Since $\mathbf{u}(\mathbf{x}, t)$ in Eq. (1) is a real variable,

$$\hat{u}_{\mathbf{k}} = \hat{u}^*{}_{\mathbf{k}},$$

where the asterisk indicates the complex conjugate, we restrict the wavevectors to a subset of $\mathbb{Z}^2$ defined by

$$\mathbb{K}^2 \equiv \{\mathbf{k} \in \mathbb{Z}^2 : k_x > 0\} \cup \{\mathbf{k} \in \mathbb{Z}^2 : k_x = 0 \wedge k_y > 0\}.$$

In addition, we define

$$\bar{\mathbf{k}} \equiv \begin{cases} \mathbf{k} & : \mathbf{k} \in \mathbb{K}^2 \\ -\mathbf{k} & : \mathbf{k} \notin \mathbb{K}^2 \end{cases} \tag{11}$$

and

$$\mathrm{sgn}(\mathbf{k}) \equiv \frac{\mathbf{k} \cdot \bar{\mathbf{k}}}{k^2}. \tag{12}$$

Introducing Eqs. (11) and (12) into Eq. (10), and separating into real and imaginary parts, we obtain the following set of ordinary differential equations (ODEs)[12]

$$\frac{du^R_{\mathbf{k}}}{dt} = -\frac{1}{\mathrm{Re}} k^2 u^R_{\mathbf{k}} + f^R_{\mathbf{k}} + \sum_{\substack{\mathbf{p} \in \mathbb{K}^2, \\ \mathbf{p} \neq \mathbf{k}}} (\mathbf{e}_{\mathbf{p}} \cdot \mathbf{k})\{(\mathbf{e}_{\overline{\mathbf{k}\ \mathbf{p}}} \cdot \mathbf{e}_{\mathbf{k}})[\mathrm{sgn}(\mathbf{k} - \mathbf{p}) u^R_{\mathbf{p}} u^I_{\overline{\mathbf{k}\ \mathbf{p}}} + u^I_{\mathbf{p}} u^R_{\overline{\mathbf{k}\ \mathbf{p}}}] + (\mathbf{e}_{\mathbf{k}+\mathbf{p}} \cdot \mathbf{e}_{\mathbf{k}})[u^R_{\mathbf{p}} u^I_{\mathbf{k}+\mathbf{p}} - u^I_{\mathbf{p}} u^R_{\mathbf{k}+\mathbf{p}}]\}, \tag{13}$$

$$\frac{du^I_{\mathbf{k}}}{dt} = -\frac{1}{\mathrm{Re}} k^2 u^I_{\mathbf{k}} + f^I_{\mathbf{k}} - \sum_{\substack{\mathbf{p} \in \mathbb{K}^2, \\ \mathbf{p} \neq \mathbf{k}}} (\mathbf{e}_{\mathbf{p}} \cdot \mathbf{k})\{(\mathbf{e}_{\overline{\mathbf{k}\ \mathbf{p}}} \cdot \mathbf{e}_{\mathbf{k}})[u^R_{\mathbf{p}} u^R_{\overline{\mathbf{k}\ \mathbf{p}}} - \mathrm{sgn}(\mathbf{k} - \mathbf{p}) u^I_{\mathbf{p}} u^I_{\overline{\mathbf{k}\ \mathbf{p}}}] + (\mathbf{e}_{\mathbf{k}+\mathbf{p}} \cdot \mathbf{e}_{\mathbf{k}})[u^R_{\mathbf{p}} u^R_{\mathbf{k}+\mathbf{p}} + u^I_{\mathbf{p}} u^I_{\mathbf{k}+\mathbf{p}}]\}, \tag{14}$$

where $\hat{f}_{\mathbf{k}} = f^R_{\mathbf{k}} + i f^I_{\mathbf{k}}$. Following Refs. 12 and 13, we apply the external forcing to the wavevector $\mathbf{k} = (4, 1)$

$$\hat{f}_{\mathbf{k}} = \begin{cases} f^R_{(4,1)} + i f^I_{(4,1)} & : \mathbf{k} = (4, 1) \\ 0 & : \mathbf{k} \neq (4, 1) \end{cases} \tag{15}$$

and set $f^R_{(4,1)} = f^I_{(4,1)} = 0.13666$. For this type of external forcing, Eqs. (1) and (2) remain invariant with respect to the lines parallel to the external force, and can lead to the coexistence of symmetrical attractors in phase space. We solve Eqs. (13) and (14) using an isotropic truncation of wavenumbers in Fourier space, which means that the Fourier space is segmented into successive rings $n^2 - n < \mathbf{k}^2 \leq n^2 + n$, $n = 1, 2, \ldots$. The rings up to $n = 8$ are considered, which gives a set of 112 complex Fourier coefficients, and 224 ODEs after separating into real and imaginary parts. Numerical integration is performed using a fourth order Runge Kutta method.

III. LAGRANGIAN COHERENT STRUCTURES

The transport and mixing properties of a fluid can be studied following the trajectories of tracer particles advected by the fluid velocity field.[20] Neglecting molecular diffusion and assuming passive tracers (i.e., the effect of particles on the flow is negligible), the trajectory $\mathbf{x}_i$ of a particle labelled i, starting at $\mathbf{x}_{i0}$ at time t_0 is given by

$$\dot{\mathbf{x}}_i(\mathbf{x}_{i0}, t_0, t) = \mathbf{u}(\mathbf{x}_i(\mathbf{x}_{i0}, t_0, t), t), \tag{16}$$

where

$$\mathbf{x}_{i0} = \mathbf{x}_i(\mathbf{x}_{i0}, t_0, t_0). \tag{17}$$

A common approach to understand chaotic mixing of particles and transport processes in unsteady flows is through the computation of the maximum finite time Lyapunov exponent.[21–23] A brief review of this technique follows. The solution of Eq. (16) can be viewed as a mapping process that takes points from their position $\mathbf{x}_{i0}$ at time t_0 to a new position $\mathbf{x}_i$ at time $t = t_0 + \tau$, where $\tau > 0$. This process is referred to as the flow map $\phi^t_{t_0}$, and satisfies[22,23]

$$\begin{aligned} &\phi^t_{t_0} : D \to D \\ &\mathbf{x}_{i0} \to \phi^t_{t_0}(\mathbf{x}_{i0}) = \mathbf{x}_i(\mathbf{x}_{i0}, t_0, t), \end{aligned} \tag{18}$$

where $D \subset \mathbb{R}^2$ is the domain of the fluid in real space. Consider the evolution of a perturbed particle trajectory,

$$\mathbf{x}'_i = \mathbf{x}_i + \delta\mathbf{x}_0, \tag{19}$$

where $\delta\mathbf{x}_0$ is infinitesimal and arbitrarily oriented. At t, the perturbation becomes

$$\delta\mathbf{x}^t_i = \phi^t_{t_0}(\mathbf{x}'_i) - \phi^t_{t_0}(\mathbf{x}_i). \tag{20}$$

Expanding $\phi^t_{t_0}$ into a Taylor series in the neighborhood of $\mathbf{x}_i$, and neglecting the higher order terms, we obtain

$$\delta\mathbf{x}^t_i = \frac{d\phi^t_{t_0}(\mathbf{x}_i)}{d\mathbf{x}} \delta\mathbf{x}_0. \tag{21}$$

The growth of the infinitesimal perturbation will be given by

$$||\delta\mathbf{x}^t_i|| = \sqrt{\delta\mathbf{x}_0 \cdot \left(\left[\frac{d\phi^t_{t_0}(\mathbf{x}_i)}{d\mathbf{x}} \right]^T \left[\frac{d\phi^t_{t_0}(\mathbf{x}_i)}{d\mathbf{x}} \right] \delta\mathbf{x}_0 \right)}, \tag{22}$$

where the superscript T denotes the matrix transpose. Let us define a finite time version of the right Cauchy Green deformation tensor as

$$C^t_{t_0} = \left[\frac{d\phi^t_{t_0}(\mathbf{x}_i)}{d\mathbf{x}}\right]^T \left[\frac{d\phi^t_{t_0}(\mathbf{x}_i)}{d\mathbf{x}}\right]. \tag{23}$$

The tensor $C^t_{t_0}$ is symmetric and positive definite, hence it admits two real positive eigenvalues and orthogonal eigen vectors. Denote the eigenvectors of $C^t_{t_0}$ as $\xi_1(\mathbf{x}_{i0}, t_0, t)$ and $\xi_2(\mathbf{x}_{i0}, t_0, t)$ with corresponding eigenvalues $\lambda_1(\mathbf{x}_{i0}, t_0, t) < \lambda_2(\mathbf{x}_{i0}, t_0, t)$, satisfying

$$C^t_{t_0}\xi_i = \lambda_i\xi_i, \qquad i = 1, 2. \tag{24}$$

If we assume that the perturbation is aligned with the direc tion of maximum stretching, then the growth of the infinitesi mal perturbation is given by

$$||\delta\mathbf{x}^t_i|| = e^{\sigma^t_{t_0}(\mathbf{x}_i)\tau}||\delta\mathbf{x}_0||, \tag{25}$$

where

$$\sigma^t_{t_0}(\mathbf{x}_i) = \frac{1}{2\tau}\ln\lambda_2 \tag{26}$$

is the maximum FTLE. In the following, we will refer to the maximum FTLE as the FTLE. The computation of the FTLE is a common technique to detect hyperbolic LCSs, which are defined as the locally strongest repelling or attracting material surfaces over a finite time interval, act ing as barriers of particle transport. Taking $t = t_0 + \tau$ in the flow map (Eq. (18)), repelling LCSs are identified as ridges in the forward time FTLE, associated with finite time stable manifolds.[22] One can also take $t = t_0 - \tau$ in Eq. (18), in which case attracting LCSs are identified as ridges in the backward time FTLE, associated with finite time stable manifolds.

We compute $\sigma^t_{t_0}$ by first covering the $[0, 2\pi] \times [0, 2\pi]$ do main with an equally spaced grid of size 512×512. At each point of the grid, we place four particles perturbed in the x and y directions following Eq. (19) where the perturbation $\delta\mathbf{x}_0$ is given by

$$\delta\mathbf{x}_0 = \{(\Delta, 0), (-\Delta, 0), (0, \Delta), (0, -\Delta)\}. \tag{27}$$

In our case, $\Delta = 2\pi/1024$. The trajectory of each perturbed particle is followed by solving Eq. (16). After that, we use the resulting trajectories to solve Eq. (23) using a finite differences method.

The FTLE is a relatively simple technique frequently used to identify hyperbolic LCSs as ridges of the for ward and backward FTLE. However, simple counterex amples demonstrate that not all ridges of the FTLE field are hyperbolic LCSs, and LCSs need not be ridges of the FTLE field.[23] As a result, FTLE ridges can yield both false negatives and false positives in the detection of LCS.[23,25]

A mathematical theory of hyperbolic LCSs was devel oped by Haller[23] and Farazmand and Haller.[24] A numerical implementation of this theory was presented by Farazmand and Haller,[26] which allows to extract LCS as smooth, para metrized curves in two dimensional flows, and is briefly described as follows. Hyperbolic LCSs can be extracted from trajectories of the ODE defined by the first eigenvector of the Cauchy Green deformation tensor

$$\mathbf{r}' = \xi_1(\mathbf{r}), \tag{28}$$

Trajectories of Eq. (28) are referred as strainlines.[26] A com pact segment γ_0 of a strainline qualifies as a LCS if the fol lowing is satisfied for all $\mathbf{x}_0 \in \gamma_0$

1. $\lambda_1(\mathbf{x}_0) \neq \lambda_2(\mathbf{x}_0) > 1$.
2. $\langle\xi_2(\mathbf{x}_0), \nabla^2\lambda_2\xi_2(\mathbf{x}_0)\rangle \leq 0$.
3. $\xi_1(\mathbf{x}_0) \parallel \gamma_0$.
4. The averaged repulsion rate $\bar{\lambda}_2(\gamma)$, which is the average of λ_2 over a strainline segment γ_0, must be maximal among the averaged repulsion rates of all nearby curves γ satisfy ing $\gamma \parallel \xi_1(\mathbf{x}_0)$.

These conditions can be summarized as follows. Condition 1 ensures that the segment γ_0 of a strainline has a

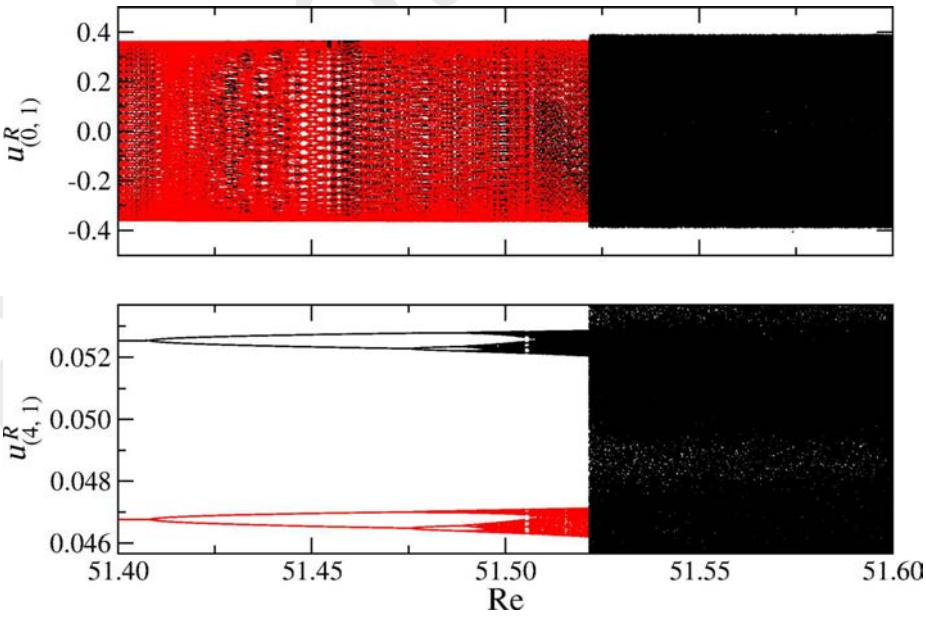

FIG. 1. Bifurcation diagram of $u^R_{(0,1)}$ (upper panel) and $u^R_{(4,1)}$ (lower panel) as a function of the Reynolds number Re, for two pre crisis attractors A_1 (black) and A_2 (red). After crisis, A_1 and A_2 merge to form an enlarged attractor (black).

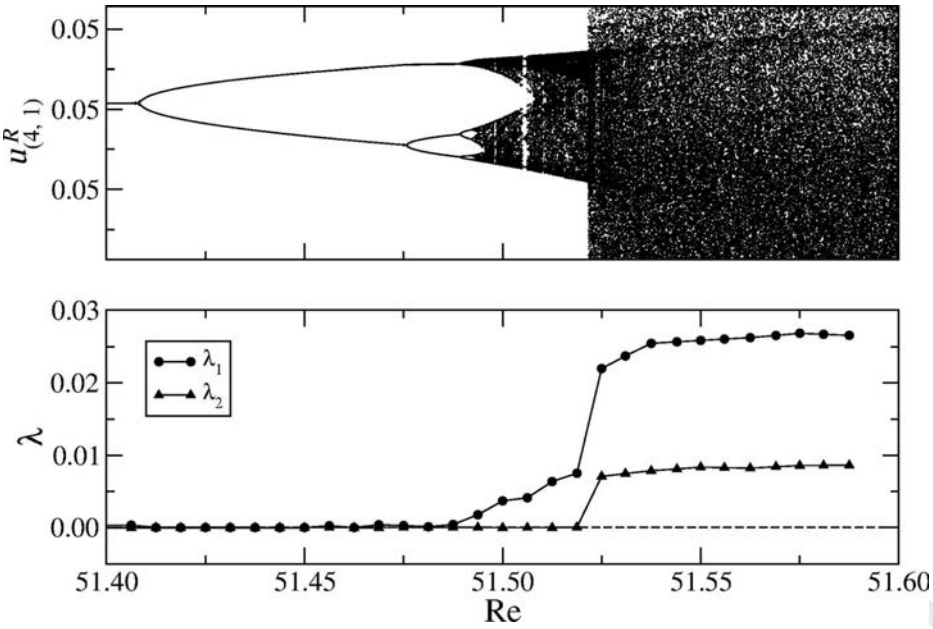

FIG. 2. Upper panel: bifurcation diagram of $u^R_{(4,1)}$ as a function of the Reynolds number Re for A_1. Lower panel: the two largest Lyapunov exponents as a function of Re.

repulsion rate normal to γ_0 (i.e., in the direction of $\xi_2(\mathbf{x}_0)$) larger than the repulsion rate in the direction tangent to γ_0 (i.e., in the direction of $\xi_1(\mathbf{x}_0)$). This condition guarantees that the detected LCSs are hyperbolic (repelling material lines) and not elliptic or parabolic (e.g., due to shear). Conditions 3 and 4 ensure that the repulsion rate normal to γ_0 has a local extremum along the LCS relative to all nearby material lines, and condition 2 ensures that this extremum is a strict local maximum.[26]

In this paper, we follow the numerical implementation presented by Farazmand and Haller[26] to detect hyperbolic LCS. We solve Eq. (28) using a fourth order Runge Kutta method with a step of 0.01. Since small scale LCSs are expected to have a negligible effect on the resulting pattern of the flow, we discard LCSs with length smaller than a suitable threshold following Farazmand and Haller.[26]

IV. EULERIAN CHAOS

A. Bifurcation diagram and attractors

We begin our nonlinear analysis by constructing a bifurcation diagram for the solution of Eqs. (13) and (14) as a function of the Reynolds number Re. This diagram was constructed by defining a Poincaré hyperplane as $u^R_{(8,2)} = -0.0002$, and

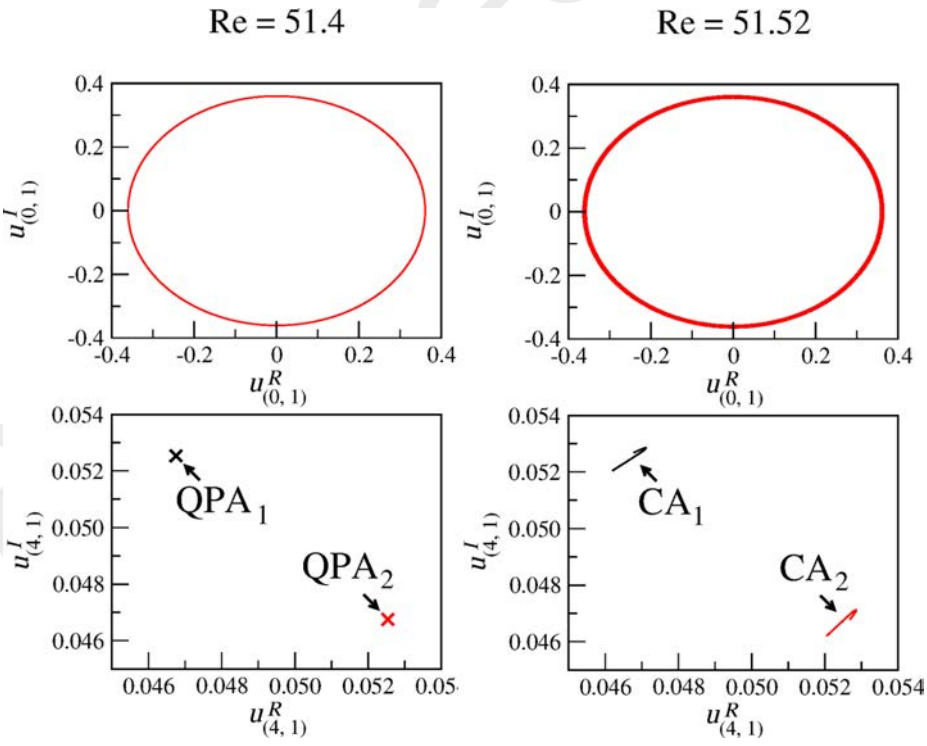

FIG. 3. Poincaré points of the quasiperiodic attractors QPA_1 (black) and QPA_2 (red) for Re 51.4 (left side panels) and chaotic attractors CA_1 and CA_2 for Re 51.52 (right side panels) projected using Fourier modes $\hat{u}_{(0,1)}$ and $\hat{u}_{(4,1)}$.

plotting the intersections between the trajectory and the Poincaré hyperplane where $du^R_{(8,2)}/dt > 0$. In the following, we will refer to these intersections as the "Poincaré points." Figure 1 shows the bifurcation diagram using two different projections, the real part of $\hat{u}_{(0,1)}$ (upper panel) and the real part of the forced mode $\hat{u}_{(4,1)}$ (lower panel). Starting from $\mathrm{Re} = 51.40$, there is a coexistence of two attractors, denoted A_1 (black) and A_2 (red). Depending on the initial condition, the dynamics of Eqs. (13) and (14) can converge to A_1 or A_2. From the upper panel of Fig. 1, it seems that the two attractors occupy the same region, and that the two attractors maintain the same dynamics with increasing Re, up to the critical value $\mathrm{Re} = \mathrm{Re}_c \sim 51.5216$, where they merge and form an enlarged chaotic attractor. However, several hidden features of the bifurcation diagram are unveiled by the projection onto the forced mode, shown in the lower panel of Fig. 1, in which the two coexisting attractors can be clearly distinguished. At $\mathrm{Re} = 51.40$, the computation of the two largest Lyapunov exponents λ_1 and λ_2 using the method described by Benettin *et al.*[27] gives $\lambda_1 = \lambda_2 = 0$ for A_1 and A_2, which indicates that the dynamics of the two coexisting attractors is quasiperiodic. At $\mathrm{Re} \sim 51.41$, a quasiperiodic doubling bifurcation occurs for A_1 and A_2. This bifurcation occurs when a quasiperiodic attractor loses stability, and a new quasiperiodic attractor is created with one fundamental frequency which is half the fundamental frequency of the previous quasiperiodic attractor.[28–30] Quasiperiodic doubling bifurcations have also been observed in numerical studies of low dimensional models of the 2D Navier Stokes equations[31] and in simulations of three dimensional highly symmetric flows.[30] As the Reynolds number is increased, the two attractors undergo a cascade of quasiperiodic doubling bifurcations until $\mathrm{Re} \sim 51.49$ where A_1 and A_2 become chaotic. At $\mathrm{Re} \sim 51.5216$, the two attractors merge and form an enlarged chaotic attractor in a crisis like transition. Note that the scale of the vertical axis in the bottom panel of Fig. 1 is smaller than the size of the enlarged chaotic attractor. This scale was chosen to show clearly the coexistence of A_1 and A_2 before Re_c, and the quasiperiodic doubling bifurcations.

We compute the two largest Lyapunov exponents λ_1 and λ_2 to characterize the different flow regimes shown in the bifurcation diagram as a function of Re. Since for $\mathrm{Re} < \mathrm{Re}_c$ the evolution of the bifurcation diagram of the two attractors is identical we choose to display the Lyapunov exponents of A_1. The upper panel of Figure 2 shows the projection of the bifurcation diagram of A_1 onto $u^R_{(4,1)}$, and the lower panel shows the computed values of λ_1 and λ_2. From this figure, it is clear that $\lambda_1 = \lambda_2 = 0$ for $\mathrm{Re} < 51.48$, demonstrating that the dynamics in this regime are in fact quasiperiodic, and that the doubling bifurcations of A_1 and A_2 observed in the lower panel of Fig. 1 must be quasiperiodic doubling bifurcations. For $5.48 < \mathrm{Re} < 51.525$, we observe that $\lambda_1 > 0$ and $\lambda_2 = 0$, which is indicative of chaotic dynamics. For $\mathrm{Re} > 51.525$, we have $\lambda_1 > 0$ and $\lambda_2 > 0$, which indicates that the dynamics is hyperchaotic.

Next, we inspect the projections of the phase space on the Poincaré section for different values of Re. Figure 3 shows the Poincaré points of A_1 and A_2 projected on the real and imaginary parts of the complex Fourier modes $\hat{u}_{(0,1)}$ and $\hat{u}_{(4,1)}$. For $\mathrm{Re} = 51.4$ (left hand side panels), the Poincaré points of A_1 (black) and A_2 (red) projected onto $\hat{u}_{(0,1)}$ form a closed curve, which is a typical feature of a quasiperiodic attractor. Note that, in this projection, it is apparent that A_1 and A_2 occupy the same region of phase space, and as a result, only the Poincaré points of A_2 become visible. The projection onto the Fourier mode $\hat{u}_{(4,1)}$ clearly shows that A_1 and A_2 occupy different regions of phase space, and that each quasiperiodic attractor is represented by a single point. This indicates that the quasiperiodic attractor can be classified as a nongeneric torus in which the trajectory of the attractor projected on the forcing mode displays a periodic orbit, whereas the other modes display quasiperiodic orbits with two frequencies, namely, one lower frequency related to a travelling wave, and one higher frequency related to the frequency of the forcing mode[12,13] (see Appendix B). The nongeneric torus in Fourier space generates a modulated travelling wave in real space.[12,13] The right hand side panels of Fig. 3 shows the Poincaré points of A_1 and A_2 for $\mathrm{Re} = 51.52$, in the chaotic regime, hereafter denoted by CA_1 and CA_2, respectively. The two coexisting chaotic

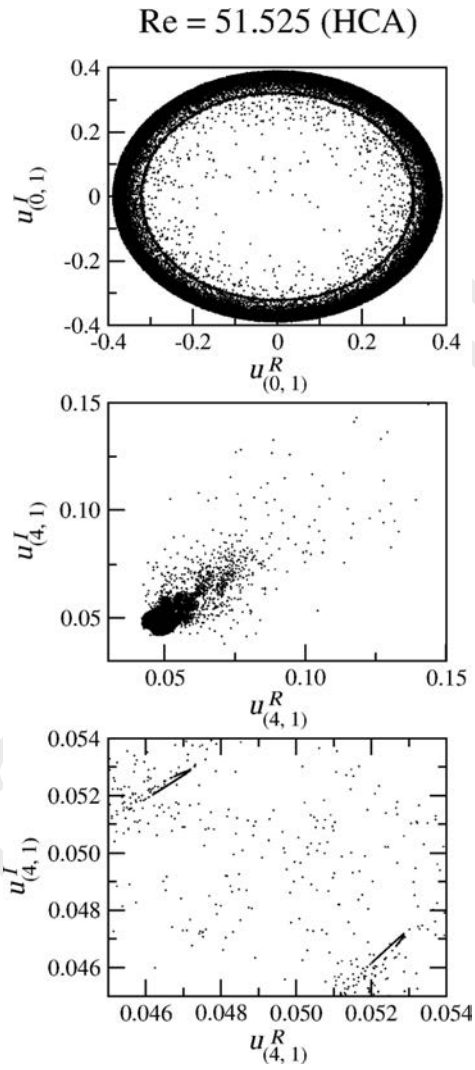

FIG. 4. Poincaré points of the HCA in the hyperchaotic regime projected using Fourier modes $\hat{u}_{(0,1)}$ (upper panel) and $\hat{u}_{(4,1)}$ (middle panel). The lower panel shows an enlargement of the hyperchaotic attractor projected using Fourier mode $\hat{u}_{(4,1)}$.

attractors can be clearly distinguished in the lower panel. Note that the two attractors are symmetric with respect to the line $u^I_{(4,1)} = u^R_{(4,1)}$. This is due to a reflection symmetry of the 2D NSE with respect to the lines parallel to the external force (Eq. (15)) where the modulus of the force is maximal.[13] Symmetric solutions have been previously reported in numerical studies of the 2D NSE with periodical boundary conditions and constant single mode forcing[12–14] and in numerical simulations of the three dimensional Rayleigh Bènard convection.[32]

The bifurcation diagrams shown in Figs. 1 and 2 indicate that at $\mathrm{Re} = \mathrm{Re}_c \sim 51.5216$ the attractors CA_1 and CA_2 merge to form a HC attractor (HCA). The Poincaré points of the enlarged attractor at $\mathrm{Re} = 51.525 > \mathrm{Re}_c$ projected on the Fourier modes $\hat{u}_{(0,1)}$ and $\hat{u}_{(4,1)}$ are shown in the upper and middle panels of Figure 4, respectively. Evidently, the HCA occupies a larger region of phase space. A detailed view of the projection on mode $\hat{u}_{(4,1)}$ is shown in the lower panel of Fig. 4. Comparing with the lower, right hand side panel of Fig. 3, it becomes clear that A_1 and A_2 are merged into the HCA.

B. Chaotic saddles

The left side panels of Figure 5 show that, prior to the transition to hyperchaos, the time series of the kinetic energy

$$E(t) = \frac{1}{(2\pi)^2}\int_0^{2\pi}\int_0^{2\pi} u^2(\mathbf{x},t)dxdy, \tag{29}$$

and the enstrophy

$$\Omega(t) = \frac{1}{(2\pi)^2}\int_0^{2\pi}\int_0^{2\pi} \omega^2(\mathbf{x},t)dxdy, \tag{30}$$

where $\omega = \nabla \times \mathbf{u}$ is the vorticity, display chaotic transients before the trajectory converges to either CA_1 or CA_2. The dynamics of the chaotic transient shows higher variability than the regular dynamics of the asymptotic state, and sudden decreases of kinetic energy associated with strong "bursts" of enstrophy occur intermittently. This behavior strongly resembles the dynamics of the hyperchaotic attractor (right side panels of Fig. 5), in which the time series randomly alternates between dynamics resembling the "laminar" behavior prior to Re_c, and dynamics with higher variability and intermittent "bursts."

The chaotic transients shown in the left side panels of Figure 5 are due to the presence of a chaotic saddle in phase space. We use the sprinkler method to find chaotic saddles.[5,6] This method works by defining a restraining region in the Poincaré section which contains a chaotic saddle and no attractor. The trajectory of any initial condition arbitrarily close to the chaotic saddle will eventually leave the restraining region, except for initial conditions located exactly in the chaotic saddle or its stable manifold. Define the escape time as the time it takes for a trajectory to leave this region. The restraining region is covered by a grid of initial conditions, and the trajectory of each initial condition is followed until some time t_c which should be larger than the average escape time from the restraining region, and must be adjusted after some trial and error. We define the restraining region by covering the Poincaré points of CA_1, projected using the real and imaginary parts of the forced mode $\hat{u}_{(4,1)}$, with two narrow boxes superposing the upper and the lower part of the attractor. A similar region was defined for the CA_2 attractor. We select those trajectories that remain in the restraining region after $t_c = 16585$ time units, and plot the Poincaré points obtained at $t = 0.5t_c = 8292.5$ which approximate the

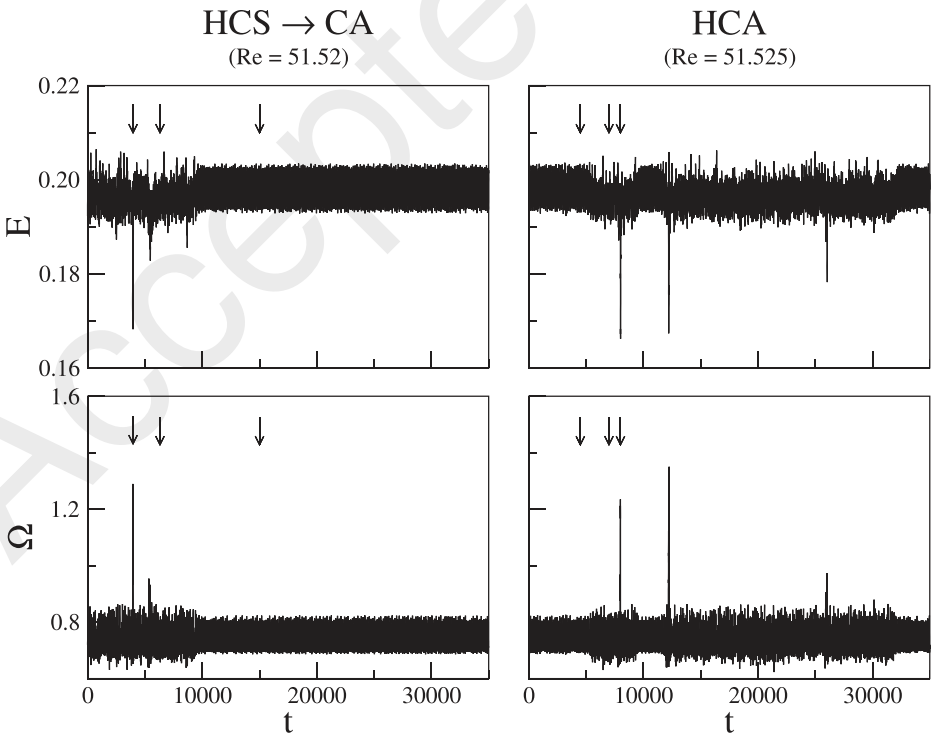

FIG. 5. Time series of the kinetic energy E (upper panels) and the enstrophy Ω (lower panels) in the chaotic regime (Re 51.52) and the hyperchaotic regime (Re 51.525). The arrows indicate the selected values of t used to detect Lagrangian coherent structures (Figs. 8 and 9).

chaotic saddle.[5,6] The left side panels of Fig. 6 show the Poincaré points of a chaotic saddle (gray) superposed by the Poincaré points of the chaotic attractors CA_1 (black) and CA_2 (red), for $Re = 51.52 < Re_c$, and projected onto Fourier modes $\hat{u}_{(0,1)}$ (upper panel) and $\hat{u}_{(4,1)}$ (middle panel). The bottom panel shows an enlarged view of the $\hat{u}_{(4,1)}$ projection, clearly showing the coexistence of CA_1, CA_2, and the chaotic saddle. We used the stagger and step algorithm[33] to compute the two largest Lyapunov exponents of this chaotic saddle, and obtained the values $\lambda_1 = 0.026$ and $\lambda_2 = 0.008$. Hence, we call this chaotic saddle a HC saddle (HCS). The HCS governs the dynamics of chaotic transients in the time series of the kinetic energy and enstrophy before converging to either CA_1 or CA_2, as exemplified in the left side panels of Fig. 5. A comparison between the HCS and the HCA shown in Fig. 4 indicates that, after the crisis, the two chaotic attractors merge with the HCS, which explains the sudden creation of an enlarged attractor.

The right side panels of Fig. 6 show the Poincaré points of the HCS and two chaotic saddles found after applying the sprinkler method for $Re = 51.525 > Re_c$. These two chaotic saddles are located within the same region in phase space previously occupied by CA_1 and CA_2 prior to the transition. For this reason, the chaotic saddles are properly referenced as CS_1 and CS_2. They are the continuation of CA_1 and CA_2 in the hyperchaotic regime, after losing stability and becoming nonattracting chaotic sets. This change of stability (i.e., the transition from an attracting chaotic set with a corresponding basin of attraction to a nonattracting chaotic set with an associated fractal stable manifold) explains the small "gaps" or empty spaces which appear in the Poincaré projections of both CS_1 and CS_2. From the right side panels of Fig. 6, it becomes clear that the HCA shown in Fig. 4 is composed by the HCS, CS_1, and CS_2. In this regime, the CS_1 and the CS_2 are responsible for the laminar intervals shown in the time series of the right side panels of Fig. 5, while the HCS governs the dynamics with higher variability and occasional "bursts" which appear intermittently in the time series of the enstrophy of Fig. 5 for $Re = 51.525 > Re_c$. This scenario is the same described by Szabó and Tél[34] for temporal

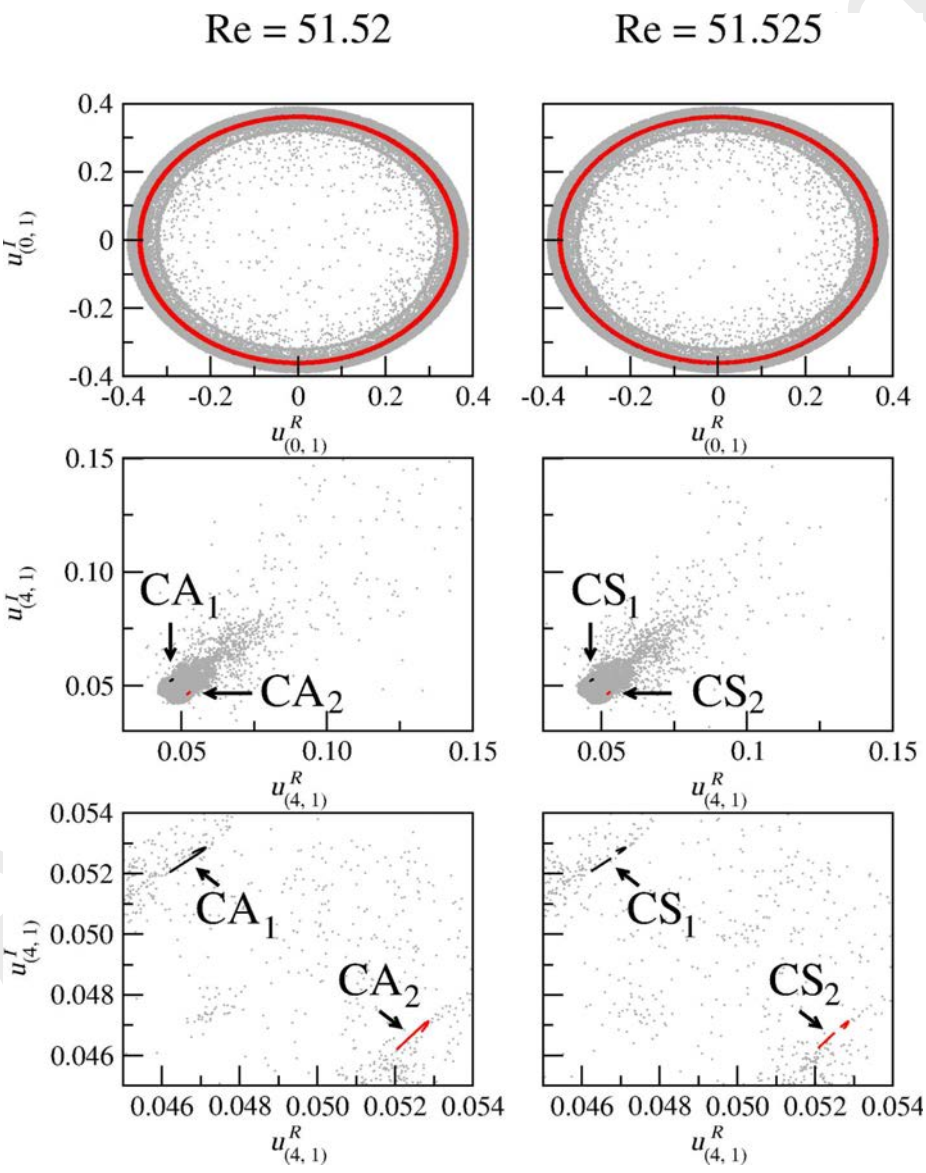

FIG. 6. Left side panels: Poincaré points of the HCS (gray) and chaotic attractors CA_1 (black) and CA_2 (red) in the chaotic regime (Re 51.52) projected using Fourier modes $\hat{u}_{(0,1)}$ (upper panels) and $\hat{u}_{(4,1)}$ (middle panels). The lower panel shows an enlargement of the middle panel. Right side panels: Poincaré points of the HCS (gray), and chaotic saddles CS_1 (black) and CS_2 (red), in the hyperchaotic regime (Re 51.525).

chaos and by Rempel and Chian[1] for one dimensional spatio temporal chaos.

V. LAGRANGIAN CHAOS

The Lagrangian techniques discussed in Sec. III require the integration of particle trajectories backwards in time when $t = t_0 - \tau$. To avoid numerical instabilities, we choose to interpolate recorded datasets of our numerical results. The datasets consist of snapshots of the velocity field in real space recorded every 0.1 time units. Following Mendoza and Mancho,[35] we use third order Lagrange polynomials for interpolation in time. We interpolate in space using Hermite polynomials which is a third order interpolation scheme commonly used for the integration of particle trajecto ries.[21,22,36] We plot the resulting values of Eq. (26) against the initial condition of the respective particle, resulting in a scalar field. The "FTLE field" is obtained by representing the numerical values of the backward time FTLE using a colour scale varying from black (smaller values) to red (larger val ues), and the forward time FTLE is represented using a col our scale from black (smaller values) to green (large values). After that, the forward and backward time FTLE are merged to form a three vector red green blue image for visualization.

Choosing an optimal value of τ will depend on the sys tem being studied. A small value of τ will not allow the for mation of patterns in the FTLE field and LCSs, whereas a large value of τ implies a higher computational effort and larger amount of recorded datasets. Also, one of the prob lems with large τ is that the FTLE plots may become increas ingly complex, with material lines "growing" and filling the entire phase space, rendering difficulty in the distinction between regimes. Basically, smaller values of τ enable the detection of the main (most attracting/repelling) LCSs, which organize transport between different regions of the flow, and larger τ reveals the structures which will affect the system only at later times. Figure 7 shows the forward time FTLE field superposed by hyperbolic LCSs obtained by solv ing Eq. (28) and checking conditions 1 4 indicated in Sec. III, for Re = 51.52, $t = 15\,000$, and two different values of τ. The upper panel shows the resulting pattern for $\tau = 5$ and the lower panel displays the pattern for $\tau = 10$. The spatio temporal patterns can be clearly distinguished in the lower panel. Note that the intermittent bursts in Fig. 5 are short time events with a typical duration of 20 23 time units. Therefore, we avoid the overlapping of intervals with differ ent dynamics by setting $\tau = 10$, which allows us to identify the main LCSs.

Figure 8 shows the FTLE field computed from the HCA after transition, corresponding to the time series of kinetic energy and enstrophy shown in the right side of Fig. 5. The upper panel corresponds to an interval $[t_0 - \tau, t_0 + \tau]$ at $t_0 = 4500$, the middle panel corresponds to $t_0 = 7000$, and the lower panel corresponds to $t_0 = 8005$. The selected val ues of t_0 are indicated by arrows in Fig. 5. On each panel, the FTLE field is superposed by hyperbolic LCSs obtained by solving Eq. (28) and checking conditions 1 4 indicated in Sec. III. The backward time LCSs are represented by white

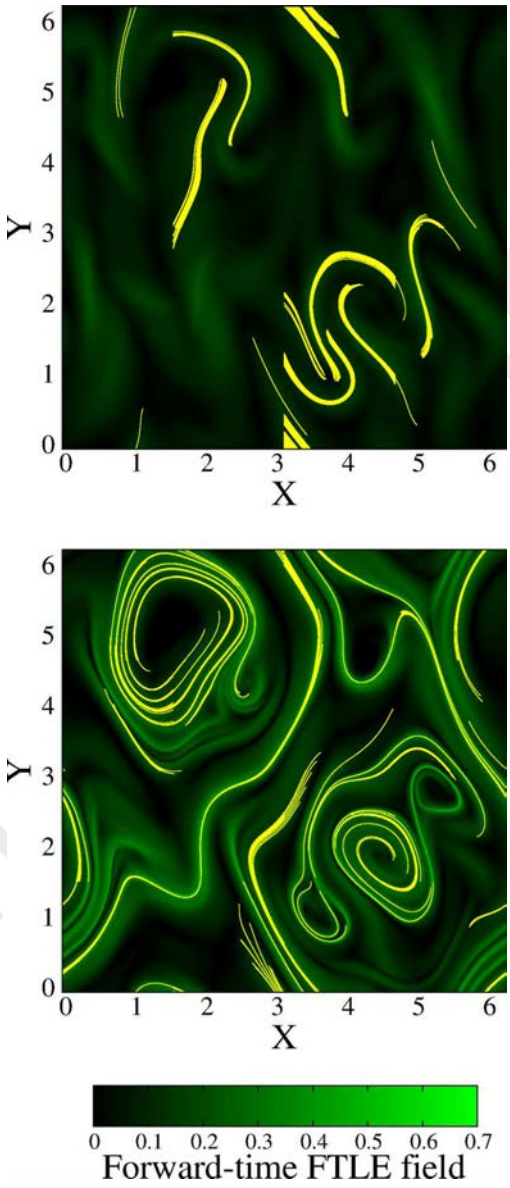

FIG. 7. The forward time FTLE field of Re 51.52 at t 15 000 for τ 5 (upper panel), and τ 10 (lower panel), superposed by forward time hyper bolic LCSs (yellow lines).

lines, whereas the forward time LCSs are indicated by yel low lines. The upper panel represents a laminar period, in which the spatiotemporal patterns of the FTLE field are organized by several large scale vortices surrounded by hyperbolic LCS. The middle panel represents a period of higher variability than the laminar period in the time series of Fig. 5. The spatiotemporal patterns displayed by the FTLE field and highlighted by the hyperbolic LCSs are simi lar to the laminar period. The difference between the upper and the middle panels of Fig. 8 becomes clear in the statistics of the FTLE field, which will be discussed later. The lower panel depicts the FTLE field during a burst, showing a sud den increase in the complexity of the entanglement of mate rial lines, accounting for a higher degree of disorder in space and time. From Fig. 8, we can conclude that the intermittent bursts observed in the time series of Fig. 5 after the transition

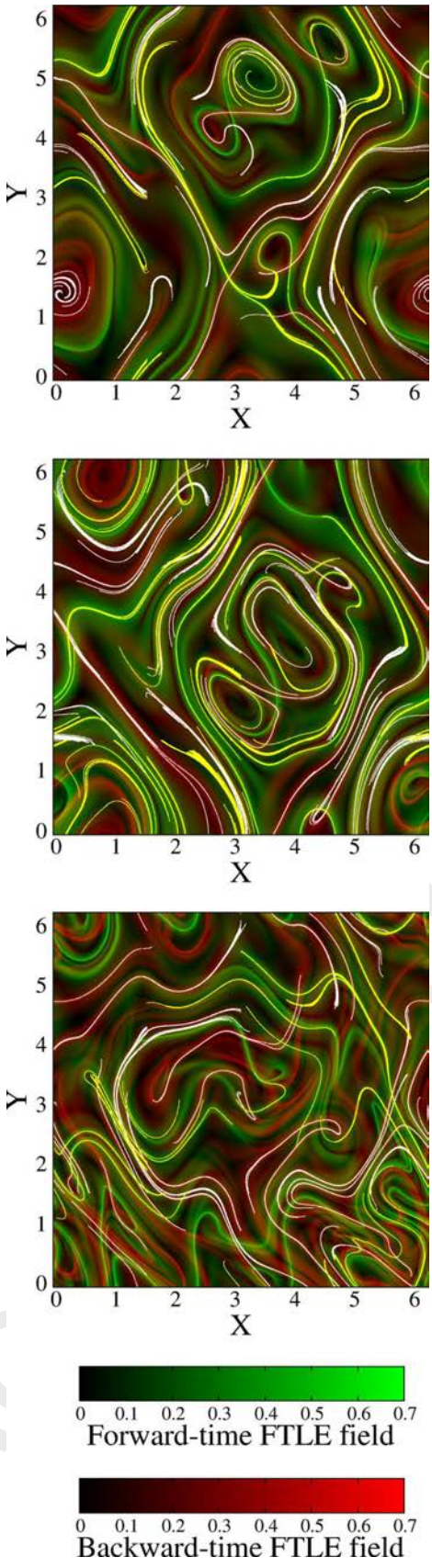

FIG. 8. The FTLE field of the hyperchaotic attractor (Re 51.525) at t 4500 (upper panel), t 7000 (middle panel), and t 8500 (bottom panel), superposed by forward time LCSs (yellow) and backward time LCSs (white).

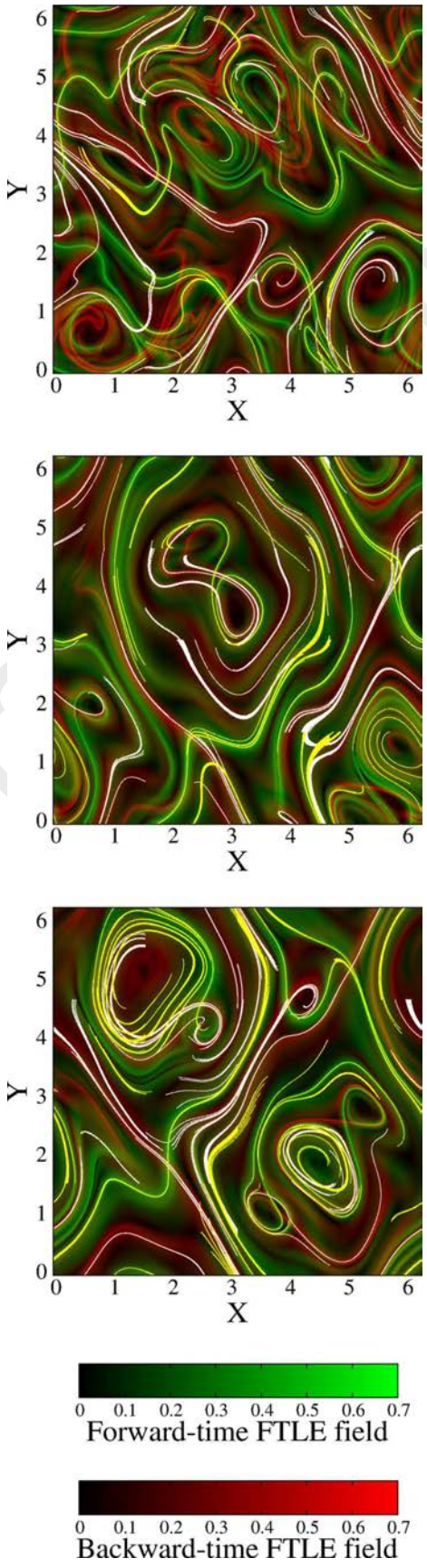

FIG. 9. The FTLE field for Re 51.52, at t 3960 (upper panel), t 6316 (middle panel), and t 15 000 (bottom panel), superposed by forward time LCSs (yellow) and backward time LCSs (white).

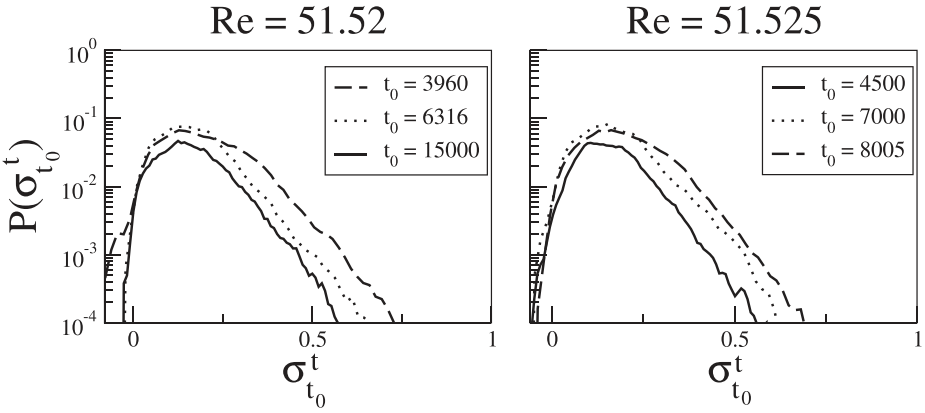

FIG. 10. Probability distribution function of the FTLE field for Re $51.52 < \mathrm{Re}_c$ (left side panels) and Re $51.525 > \mathrm{Re}_c$ (right side panels). The continuous line represents laminar periods, the dotted line corresponds to the high variability periods, and the dashed line represents strong bursts.

to hyperchaos are responsible for episodic enhancements of the fluid complexity.

Recall that, before the transition to hyperchaos, the chaotic transients are governed by a hyperchaotic saddle. Figure 9 shows the FTLE field and hyperbolic LCSs for $\mathrm{Re} = 51.52 < \mathrm{Re}_c$, at three different values of t_0 indicated by arrows in the time series shown in the left side panels of Fig. 5. The upper panel corresponds to the middle of a burst at $t_0 = 3960$, the middle panel corresponds to $t_0 = 6316$, and the lower panel represents the dynamics after converging to the CA_1 at $t_0 = 15\,000$. The upper panel indicates that the bursty behavior of the HCS is characterized by irregular patterns of the FTLE field and hyperbolic LCSs, similarly to the burst of the HCA shown in the lower panel of Fig. 8. The spatiotemporal patterns of the middle and bottom panels resemble the patterns of the middle and upper panels of Fig. 8, respectively.

The spatiotemporal patterns of Figs. 8 and 9 can be compared quantitatively by constructing the probability distribution function (PDF) of the FTLE field.[37,38] The left side panel of Fig. 10 shows the PDF of the backward time FTLE field $\sigma^t_{t_0}$ computed from chaotic saddles for $\mathrm{Re} = 51.52 < \mathrm{Re}_c$. The dashed line represents the strong burst during the chaotic transient around $t_0 = 3960$ (see Fig. 6), the dotted line corresponds to $t_0 = 6316$, and the continuous line corresponds to the laminar period after convergence to CA_1 ($t_0 = 15\,000$). All PDFs exhibit an asymmetric shape with a fat tail towards large values of $\sigma^t_{t_0}$. A similar shape was observed by Ref. 37 for the backward time FTLE computed from velocity fields of surface ocean currents inferred using satellite data. Clearly, the PDF is narrower during the laminar period, and becomes broader during the burst period. This figure allows for a clear differentiation between the laminar state at $t_0 = 15\,000$ and the high variability state at $t_0 = 6316$ with a slightly broader PDF compared to the laminar PDF.

The right side panels of Fig. 10 show the PDFs of the backward time $\sigma^t_{t_0}$ for $\mathrm{Re} = 51.525 > \mathrm{Re}_c$. The laminar state at $t = 4500$ is represented by a continuous line, the higher variability state at $t = 7000$ is represented by a dotted line, and the strong burst observed at $t = 8005$ is represented by a dashed line. The shape and width of the PDF of each state are very similar to the corresponding PDF prior to the transition to HCA. From this figure, we conclude that the spatiotemporal patterns of the flow after transition to hyperchaos can be predicted by the hyperchaotic transient observed before the transition, in agreement with the conclusion of Rempel and Chian[1] for a one dimensional regularized long wave equation.

VI. CONCLUSION

In this paper, we performed numerical simulations of the two dimensional incompressible Navier Stokes equations with external forcing and periodic boundary conditions. By constructing bifurcation diagrams, we showed the transition from a quasiperiodic regime to a chaotic regime, and then to a hyperchaotic regime with increasing Reynolds number. Prior to the transition to hyperchaos, we show that the chaotic transient observed in the time series of the kinetic energy and enstrophy is due to the presence of a hyperchaotic saddle. After transition, there is chaos hyperchaos intermittency due to the coupling between the hyperchaotic saddle and two chaotic saddles, which are the continuation of the two symmetric chaotic attractors CA_1 and CA_2. The Lagrangian mixing properties of the fluid were characterized using the FTLE field and a mathematical theory recently developed to detect LCSs as parametrized curves in 2D flows. The laminar periods associated with the chaotic saddles CS_1 and CS_2 display smoother patterns of the FTLE field, and are organized by several large scale vortices surrounded by hyperbolic LCSs. In contrast, during the bursty periods there is a sudden increase on the fluid complexity associated with the hyperchaotic saddle. The PDFs of the backward time FTLE field demonstrate that the enhanced complexity of the spatiotemporal patterns during the intermittent bursts after transition can be predicted by the hyperchaotic saddle prior to the transition, in agreement with the conclusion of Rempel and Chian.[1] To our knowledge, this is the first time that chaotic saddles at the onset of hyperchaos are related to the phenomenology of chaotic advection, with emphasis on hyperbolic LCSs.

In this paper, we focused on the transition to hyperchaos by varying the Reynolds number and fixing the size of the physical domain. As stated in Sec. II, by choosing $L_x = L_y = 2\pi$ the wavevector $\mathbf{k} \in \mathbb{Z}^2$, which simplifies the numerical implementation. Several studies have investigated the scaling properties of transient chaos with the size of the system in partial differential equations.[9,39,40] Although this type of investigation is outside the scope of the present paper, it is an interesting topic of research for future work. In addition,

we have restricted our Lagrangian analysis to hyperbolic LCSs detected using the computational framework presented by Farazmand and Haller.[26] A unified theory of LCSs that allows the identification of hyperbolic, parabolic, and elliptic barriers of flows was developed recently by Haller and Berón Vera.[41] A complete Lagrangian characterization at the onset of hyperchaos using this theory, and a quantification of the degree of Lagrangian chaos before and after transition using the concept of LCS cores developed by Olascoaga and Haller[42] will be the topic of a future paper.

The transition to hyperchaos described in this paper has a strong similarity with the onset of spatiotemporal chaos reported in a number of numerical simulations of nonlinear partial differential equations.[1,3,4,7] However, we were unable to observe a transition from narrow band to broad band power spectrum in the wavenumber domain, which is a characteristic of STC, due to the regime of low Reynolds number studied in this paper. Nonetheless, the Lagrangian techniques studied in this paper are applicable to high Reynolds number fluid turbulence where spatiotemporal chaos is expected.

ACKNOWLEDGMENTS

The authors thank the reviewers for valuable comments. This work was supported by CNPq, FAPESP and DPP/UnB. A.C.L.C. is grateful for the award of a Marie Curie International Incoming Fellowship and the hospitality of Paris Observatory. B.A.T. is thankful for the financial support of FONDECyT Grant No. 1130273.

APPENDIX A: DECOUPLING OF k = 0

In Sec. II, we made the restriction $\mathbf{k} \neq 0$ in the Fourier series because $\hat{\mathbf{u}}_0$ is decoupled from the evolution equations. This can be elucidated after substituting Eqs. (3) (5) into Eq. (1)

$$\sum_{\substack{\mathbf{k}\in\mathbb{Z}^2,\\ \mathbf{k}\neq 0}} \left(\frac{d\hat{\mathbf{u}}_\mathbf{k}}{dt}\right) e^{i\mathbf{k}\cdot\mathbf{x}} = -i \sum_{\substack{\mathbf{k}\in\mathbb{Z}^2,\\ \mathbf{k}\neq 0}} \mathbf{k}\hat{p}_\mathbf{k} e^{i\mathbf{k}\cdot\mathbf{x}} - \frac{1}{\mathrm{Re}} \sum_{\substack{\mathbf{k}\in\mathbb{Z}^2,\\ \mathbf{k}\neq 0}} k^2 \hat{\mathbf{u}}_\mathbf{k} e^{i\mathbf{k}\cdot\mathbf{x}} + \sum_{\substack{\mathbf{k}\in\mathbb{Z}^2,\\ \mathbf{k}\neq 0}} \hat{\mathbf{f}}_\mathbf{k} e^{i\mathbf{k}\cdot\mathbf{x}} - i \sum_{\substack{\mathbf{p}\in\mathbb{Z}^2,\\ \mathbf{p}\neq 0}} \sum_{\substack{\mathbf{q}\in\mathbb{Z}^2,\\ \mathbf{q}\neq 0}} (\hat{\mathbf{u}}_\mathbf{p}\cdot\mathbf{k})\hat{\mathbf{u}}_\mathbf{q} e^{i(\mathbf{p}+\mathbf{q})\cdot\mathbf{x}}. \tag{A1}$$

If $\mathbf{k} = 0$, the nonlinear term vanishes, and as a result the evolution equation for $\hat{\mathbf{u}}_0$ is in fact decoupled from other Fourier modes. Moreover, our choice of the forcing term given by Eq. (15) indicates that the Fourier coefficient $\hat{\mathbf{u}}_0$ is constant in time. We set $\hat{\mathbf{u}}_0 = (0, 0)$ which is equivalent to assume a vanishing mean flow.[32]

The last term in the right hand side of Eq. (A1) will couple with the other terms only if $\mathbf{p} + \mathbf{q} = \mathbf{k}$. By inserting this constraint into Eq. (A1), one obtains Eq. (6).

APPENDIX B: NONGENERIC TORUS AT Re = 51.4

In Sec. IV, we refer to the quasiperiodic attractor at Re = 51.4 as a nongeneric torus in which the forcing mode displays a periodic orbit, whereas the other modes display quasiperiodic orbits with a low frequency component related to a travelling wave, and a high frequency component related to the frequency of the forcing mode.[12,13] This is illustrated in Fig. 11. The upper panel shows the power spectrum computed from the time series of the real part of the Fourier mode $\hat{u}_{(0,1)}$ as a function of the frequency f, and the lower panel shows the power spectrum of the real part of the forced mode $\hat{u}_{(4,1)}$. Clearly, the dynamics of the forced mode is periodic with frequency $f_2 = 0.012938208$, followed by a sequence of peaks resulting from harmonic oscillations given by nf_2, where $n = 2, 3, \ldots$. The fundamental frequency of $u^R_{(0,1)}$ in the upper panel of Fig. 11 is $f_1 = 0.000217463$, followed by a sequence of double peaks. The first pair of peaks corresponds to the frequencies $f_3 = 0.012715873 = f_2 - f_1$ and $f_4 = 0.013150800 = f_2 + f_1$, which are clearly related to the frequency of the forced mode f_2. The subsequent pairs of peaks in the upper panel of Fig. 11 correspond to oscillations with frequencies $nf_2 - f_1$ and $nf_2 + f_1$, where $n = 2, 3, \ldots$.

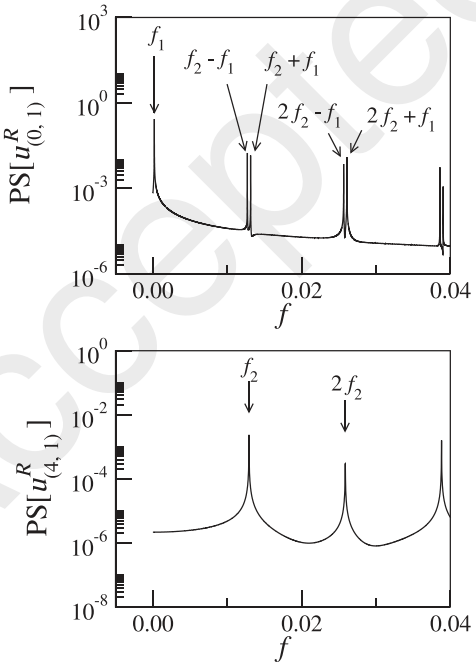

FIG. 11. Power spectra of the time series of $u^R_{(0,1)}$ (upper panel) and $u^R_{(4,1)}$ (lower panel) at Re 51.4. The frequencies indicated in the figure are f_1 0.000217463 and f_2 0.012938208.

[1] E. L. Rempel and A. C. L. Chian, "Origin of transient and intermittent dynamics in spatiotemporal chaotic systems," Phys. Rev. Lett. **98**, 014101 (2007).

[2]A. C. L. Chian, R. A. Miranda, E. L. Rempel, Y. Saiki, and M. Yamada, "Amplitude phase synchronization at the onset of permanent spatiotemporal chaos," Phys. Rev. Lett. **104**, 254102 (2010).
[3]E. L. Rempel, R. A. Miranda, and A. C. L. Chian, "Spatiotemporal intermittency and chaotic saddles in the regularized long wave equation," Phys. Fluids **21**, 074105 (2009).
[4]E. L. Rempel, A. C. L. Chian, and R. A. Miranda, "Chaotic saddles at the onset of intermittent spatiotemporal chaos," Phys. Rev. E **76**, 056217 (2007).
[5]H. Kantz and P. Grassberger, "Repellers, semi attractors, and long lived chaotic transients," Physica D **17**, 75 (1985).
[6]G. H. Hsu, E. Ott, and C. Grebogi, "Strange saddles and the dimensions of their invariant manifolds," Phys. Lett. A **127**, 199 (1988).
[7]R. Braun and F. Feudel, "Supertransient chaos in the two dimensional complex Ginzburg Landau equation," Phys. Rev. E **53**, 6562 (1996).
[8]E. L. Rempel, A. C. L. Chian, E. E. N. Macau, and R. R. Rosa, "Analysis of chaotic saddles in high dimensional dynamical systems: The Kuramoto Sivashinsky equation," Chaos **14**, 545 (2004).
[9]Y. C. Lai and T. Tél, *Transient Chaos: Complex Dynamics on Finite-Time Scales* (Springer, 2011).
[10]C. Boldrighini and V. Franceschini, "5 dimensional truncation of the plane incompressible Navier Stokes equations," Commun. Math. Phys. **64**, 159 (1979).
[11]J. Lee, "Topology of trajectories of the 2D Navier Stokes equations," Chaos **2**, 537 (1992).
[12]F. Feudel and N. Seehafer, "On the bifurcation phenomena in truncations of the 2D Navier Stokes equations," Chaos, Solitons Fractals **5**, 1805 (1995).
[13]F. Feudel and N. Seehafer, "Bifurcations and pattern formation in a two dimensional Navier Stokes fluid," Phys. Rev. E **52**, 3506 (1995).
[14]R. Braun, F. Feudel, and N. Seehafer, "Bifurcations and chaos in an array of forced vortices," Phys. Rev. E **55**, 6979 (1997).
[15]R. Braun, F. Feudel, and P. Guzdar, "Route to chaos for a two dimensional externally driven flow," Phys. Rev. E **58**, 1927 (1998).
[16]D. Molenaar, H. J. H. Clercx, and G. J. F. van Heijst, "Transition to chaos in a confined two dimensional flow," Phys. Rev. Lett. **95**, 104503 (2005).
[17]D. Ruelle and F. Takens, "Nature of turbulence," Commun. Math. Phys. **20**, 167 (1971).
[18]S. Newhouse, D. Ruelle, and F. Takens, "Occurrence of strange axiom A attractors near quasi periodic flows on T^m, $m \geq 3$," Commun. Math. Phys. **64**, 35 (1978).
[19]M. Mathur, G. Haller, T. Peacock, J. E. Ruppert Felsot, and H. L. Swinney, "Uncovering the Lagrangian skeleton of turbulence," Phys. Rev. Lett. **98**, 144502 (2007).
[20]J. M. Ottino, *The Theory of Mixing: Stretching, Chaos and Transport* (Cambridge University Press, Cambridge, England, 1989).
[21]G. Haller and G. Yuan, "Lagrangian coherent structures and mixing in two dimensional turbulence," Physica D **147**, 352 (2000).
[22]S. C. Shadden, F. Lekien, and J. E. Marsden, "Definition and properties of Lagrangian coherent structures from finite time Lyapunov exponents in two dimensional aperiodic flows," Physica D **212**, 271 (2005).
[23]G. Haller, "A variational theory of hyperbolic Lagrangian coherent structures," Physica D **240**, 574 (2011).
[24]M. Farazmand and G. Haller, "Erratum and addendum to: A variational theory of hyperbolic Lagrangian coherent structures," Physica D **241**, 439 (2012).
[25]T. Peacock and G. Haller, "Lagrangian coherent structures: The hidden skeleton of fluid flows," Phys. Today **66**(2), 41 (2013).
[26]M. Farazmand and G. Haller, "Computing Lagrangian coherent structures from their variational theory," Chaos **22**, 013128 (2012).
[27]G. Benettin, L. Galgani, A. Giorgilli, and J. M. Strelcyn, "Lyapunov characteristic exponents for smooth dynamical systems and for hamiltonian systems: A method for computing all of them. Part 1: Theory," Meccanica **15**, 9 (1980).
[28]H. W. Broer and G. B. Huitema, "Unfoldings of quasi periodic tori," J. Dynam. Diff. Eq. **7**, 191 (1995).
[29]B. L. J. Braaksma, H. W. Broer, and G. B. Huitema, "Toward a quasi periodic bifurcation theory," Mem. Am. Math. Soc. **83**, 83 (1990).
[30]L. van Veen, "The quasi periodic doubling cascade in the transition to weak turbulence," Physica D **210**, 249 (2005).
[31]V. Franceschini, "Bifurcations of tori and phase locking in a dissipative system of differential equations," Physica D **6**, 285 (1983).
[32]S. Scheel and N. Seehafer, "Bifurcation to oscillations in three dimensional Rayleigh Bènard convection," Phys. Rev. E **56**, 5511 (1997).
[33]D. Sweet, H. E. Nusse, and J. A. Yorke, "Stagger and step method: Detecting and computing chaotic saddles in higher dimensions," Phys. Rev. Lett. **86**, 2261 (2001).
[34]K. G. Szabó and T. Tél, "Transient chaos as the backbone of dynamics on strange attractors beyond crisis," Phys. Lett. A **196**, 173 (1994).
[35]C. Mendoza and A. M. Mancho, "Hidden geometry of ocean flows," Phys. Rev. Lett. **105**, 038501 (2010).
[36]E. L. Rempel, A. C. L. Chian, and A. Brandenburg, "Lagrangian coherent structures in nonlinear dynamos," Astrophys. J. **735**, L9 (2011).
[37]F. J. Berón Vera, M. J., Olascoaga, and G. J. Goni, "Surface ocean mixing inferred from different multisatellite altimetry measurements," J. Phys. Oceanogr. **40**, 2466 (2010).
[38]T. G. Shepherd, J. N. Koshyk, and K. Ngan, "On the nature of large scale mixing in the stratosphere and mesosphere," J. Geophys. Res. **105**, 12433, doi:10.1029/2000JD900133 (2000).
[39]K. Kaneko, "Supertransients, spatiotemporal intermittency, and stability of fully developed spatiotemporal chaos," Phys. Lett. A **149**, 105 (1990).
[40]A. Wacker, S. Bose, and E. Schöll, "Transient spatiotemporal chaos in a reaction diffusion model," Europhys. Lett. **31**, 257 (1995).
[41]G. Haller and F. J. Berón Vera, "Geodesic theory of transport barriers in two dimensional flows," Physica D **241**, 1680 (2012).
[42]M. J. Olascoaga and G. Haller, "Forecasting sudden changes in environmental pollution patterns," Proc. Natl. Acad. Sci. U.S.A. **109**, 4738 (2012).